NJC

ROYAL SOCIETY OF CHEMISTRY

PAPER

View Article Online
View Journal | View Issue

Cite this: *New J. Chem.*, 2024, **48**, 5589

Lysosome-targeting solid state NIR emissive donor–acceptor molecules: a study on photophysical modulation through architectural distinction†

Ashish Kumar Kushwaha,[a] Ankit Kumar Srivastava,[a] Pradeep Kumar,[b] Anjani Kumar,[a] Saripella Srikrishna[b] and Roop Shikha Singh *[a]

The prevalence of the D–A strategy in achieving red-shifted emission has been established through designing D–A molecules of D–A–D and A–D–A constructs. Architectural control over such D–A systems integrates solid state NIR emission with lysosome tracking and sets a multifarious goal of photophysical modulation in a comprehensive way. In particular, two compounds, **CPM–1** (D–A–D) and **CPM–2** (A–D–A), have been synthesized by introducing carbazole-based donors and difluoroboron acceptors. Lysosome targeting and imaging have been achieved through incorporation of a morpholine unit, which ultimately imparts viscosity sensitivity to the construct. The fluorophores exhibited significant emission in solution along with distinctive solvatochromism, viscochromism and TICT. A comparative account of these competitive photophysical properties revealed the superior charge transfer properties of the A–D–A construct (**CPM–2**), while the D–A–D molecule (**CPM–1**) was found to be a better molecular rotor with marked viscochromism. The solid state NIR emission has been found to be much more intense in **CPM–1** relative to **CPM–2,** which further highlights the influence of structural aspects on photophysical behvaiour. Theoretical studies further established the distinctive characteristics of ground and excited states in these compounds. Owing to its excellent viscochromic behvaiour, **CPM–1** has been successfully utilized in lysosome targeting in wild-type *Drosophila* fly gut tissues through co-localization studies.

Received 18th January 2024,
Accepted 26th February 2024

DOI: 10.1039/d4nj00295d

rsc.li/njc

Introduction

Lysosomes are membrane-bound organelles providing approximately 50 different types of acid hydrolases, which play important roles in the degradation of various biomacromolecules such as carbohydrates, nucleic acids, proteins, fats, and cellular components.[1–3] Lysosomes are crucial for several cellular processes, including cholesterol *in vivo* balance, autophagy, plasma membrane repair, bone and tissue remodeling, pathogen defense, cell signaling and death.[4–6] Due to the exclusive role of lysosomal transport during tumor invasion and metastasis, the effective monitoring of intracellular lysosome has emerged as a fascinating target for cancer diagnosis and treatment.[7–9] Therefore, long term and real time visualization of lysosomes is imperative in gaining a deeper understanding of lysosomerelated cancer diagnosis and treatment. In this direction, several fluorescent probes have been illustrated in the literature and various lysotrackers are commercially available. Furthermore, cancer cells are reported to have lower pH as compared to normal cells and cancer lysosomes have higher viscosity than the lysosomes of normal cells.[10–12,15,16] This fact lays down a foundation for the development of lysotrackers using pH and viscosity as potential markers leading to effective cancer cell targeting.[13–15] In this context, the development of probes sensitive towards viscosity, which can be engineered to target lysosomes through incorporation of suitable amine-based anchors[17–20] (*viz.* morpholine, piperazine *etc.*), is one of the most prevailing strategies. This strategy utilizes the positive membrane potential of the acidic lysosomes for accumulation of amine-modified probes. Furthermore, owing to their deep tissue penetration with minimal photodamage and low tissue autofluorescence in the NIR window of 650–900 nm, NIR flurophores have become a prudent choice for *in vivo* cell imaging.[21–25] Recent research has seen a great surge in

[a] *Department of Chemistry, Institute of Science, Banaras Hindu University, Varanasi-221005, U.P., India. E-mail: roopshikha22singh@gmail.com, roopshikha.singh1@bhu.ac.in*

[b] *Department of Biochemistry, Institute of Science, Banaras Hindu University, Varanasi-221005, U.P., India*

† Electronic supplementary information (ESI) available: ^{1}H, ^{13}C, ^{11}B, and ^{19}F NMR, ESI–MS, Uv-vis, and fluorescence spectra, plots and tables are provided. See DOI: https://doi.org/10.1039/d4nj00295d

exploration of lysosome-specific NIR fluorescent probes and their applications in cancer cell targeting and imaging.[26,27]

Amongst several NIR fluorescent probes based on inorganic and organic molecules, those comprising a donor–acceptor (D–A) electronic structure are particularly fascinating as these have large Stokes shifts and excellent photophysical stability.[28–31] Rational design and engineering of these D–A fluorophores can be done to improve the brightness as well as the fluorescence wavelength. Steric hindrance or AIE characteristics can be employed to improve the brightness, while the incorporation of suitable fluorphores might lead to red-shifted emission. It has further been reported that the incorporation of additional donor/acceptor groups in conventional D–A molecules can lead to more red-shifted emissions.[32,33] Keeping these points in mind we shifted our attention toward the modification of difluoroboron-coordinated β-diketonate (BF_2bdk) compounds through suitable donors and acceptors. These compounds have become indispensible tools in bioimaging applications owing to their distinctive photophysical properties, including high molar extinction coefficients, efficient solid-state emission, two photon excited fluorescence and mechanochromism.[34–42] Their ease of syntheses, high sensitivity and prompt responses have made these crucial research hotspots in recent years.[43–59] In this direction, keeping our goal of developing NIR-active biocompatible fluorphores for selective targeting and imaging of lysosomes intact, we have designed D–A based β-diketonate derivatives. Herein, carbazole has been chosen as the donor (D), while a borondifluoride core acts as the acceptor (A); thus to have substantial control over intramolecular charge transfer (ICT) the D–A skeleton has been altered with the construction of D–A–D and A–D–A scaffolds. To address the unique need for lysosomal targeting and imaging, morpholine has been incorporated to engender viscosity sensitivity. In this context, the present work details the design and synthesis of two small D–A molecules, **CPM–1** and **CPM–2** possessing D–A–D and A–D–A architectures, respectively, wherein morpholine has been appended as a pendant group through *N*-substitution of the carbazole unit. This provides us with two morpholine units in **CPM–1**, D–A–D, and one in **CPM–2**, A–D–A, giving us an opportunity to evaluate viscochromism based on the ICT character of the fluorophores. The compounds have been characterized by various spectroscopic techniques, while a detailed photophysical study {solvatochromism, viscochromism, and twisted intramolecular charge transfer (TICT)} in solution as well as the solid state has been performed to assess the effect of the D–A architecture on photophysical modeling and NIR emission. The fluorophores have been found to be emissive both in solution and the solid state. The lysosomal targeting of **CPM–1** has been realized in wild-type *Drosophila* flies (Oregon R^+ strain) through LysoTracker Green co-localization studies.

Experimental methods

Reagents

Carbazole, 4-(2-chloroethyl)morpholine hydrochloride, 1,2dibromoethane, 1-phenyl-1,3-butanedione, acetylacetone and boron trifluoride diethyl etherate were purchased from Sigma Aldrich India, TCI chemicals India and Avra chemical India. Common reagents, potassium hydroxide, sodium hydroxide, *n*-butylamine and the solvents ethyl acetate, *n*-hexane, dimethylsulphoxide (DMSO), dichloromethane (DCM), dimethylformamide (DMF), methanol *etc.* were procured from Avra Chemicals Hyderabad, India and dried and distilled following the standard literature procedures.[60] The synthetic manipulations have been performed under an oxygen-free nitrogen atmosphere and photophysical studies using spectroscopic grade solvents.

General information

^{1}H (500 MHz), and ^{13}C (125 MHz), ^{11}B and ^{19}F NMR spectra have been obtained using a JEOL AL 500 FT–NMR spectrometer at room temperature using $Si(CH_3)_4$ as an internal standard. UV–vis and emission spectra have been acquired at room temperature using a Shimadzu UV–1800 and PerkinElmer LS55 fluorescence spectrometer, respectively. Electrospray ionization mass spectrometry (ESI–MS) measurements have been made using a SCIEX X500R QTOF instruments. Time-resolved fluorescence lifetime experiments have been performed using a TCSPC system from Horiba Yovin (Delta Flex). Compounds were excited at 482 nm using a pico-second diode laser (Model: delta diode). Data analysis has been performed using decay analysis software (HORIBA Scientific: EzTime). Solid state photoluminescence has been acquired at room temperature using a WITEC alpha 300 Focus Innovation by using a pulse diode laser (wavelength = 450 nm and power = 0.250 milliwatt).

Syntheses

Synthesis of **A1**, and **A2** and 9-(2-morpholinoethyl)-9*H*-carbazole-3-carbaldehyde (**ALD–1**) was done following the literature procedure.[61–63] 9-(2-morpholinoethyl)-9*H*-carbazole-3,6-dicarbaldehyde (**ALD–2**) was synthesized following the same synthetic procedure as for **ALD–1**.

Synthesis of ALD–2

To DMF (2.92 g, 40 mmol) at 0 °C, phosphorus oxychloride (6 g, 40 mmol) was added dropwise. The solution was allowed to warm to room temperature, and 4-(2-(9*H*-carbazol-9-yl)-ethyl)morpholine (1 g, 3.56 mmol) in 1,2-dichloroethane (6 mL) was added to it. The reaction mixture was heated to 90 °C and kept at this temperature for 24 h. Afterwards the reaction mixture was poured into water and extracted with chloroform. The chloroform layer was washed with water, dried over Na_2SO_4 and the solvent was removed *in vacuo* to yield a deeply colored product, which was purified on a silica gel column using *n*-hexane/ethyl acetate (7 : 3). ^{1}H NMR ($CDCl_3$, 500 MHz, δ ppm): 2.53 (*t*, *J* = 8 Hz, 4H), 2.82 (*t*, *J* = 13.5 Hz, 2H), 3.6 (*t*, *J* = 8.5 Hz, 4H), 4.5 (*t*, *J* = 13.5 Hz, 2H), 7.5 (d, *J* = 8.5 Hz, 2H), 8.08 (d, *J* = 8.0 Hz, 2H), 8.66 (s, 2H), 10.13 (s, 2H).^{13}C NMR ($CDCl_3$, 125 MHz, δ ppm):191.61, 144.93, 130.02, 128.03, 124.41, 123.41, 109.94, 66.97, 56.78, 54.20, 41.95.

Synthesis of CPM–1

In a 50 mL round bottom flask, 2.46 mmol of **ALD–1** and 1.12 mmol of **A1** were dissolved in a minimum amount of DCM, and the flask was flushed with nitrogen. *n*–Butylamine (0.22 eq.) was then added dropwise to the reaction mixture *via* a syringe and the reaction mixture was stirred overnight at room temperature. After completion of the reaction a solid separated out, which was filtered through a Buchner funnel and washed with cold ethyl acetate and diethyl ether and dried under vacuum. This yielded **CPM–1** as a red colured solid (yield: ∼63%). ^{1}H NMR (500 MHz, DMSO-D_6, δ ppm): 8.76 (s, 1H), 8.31 (s, 1H), 8.24–8.20 (m, 2H), 8.01 (d, J = 8.9 Hz, 1H), 7.80 (d, J = 8.8 Hz, 1H), 7.74 (d, J = 8.5 Hz, 1H), 7.53 (s, 1H), 7.33 (t, J = 7.9 Hz, 1H), 7.26 (d, J = 15.3 Hz, 1H), 6.55 (d, J = 18.4 Hz, 1H), 4.86 (t, J = 6.0 Hz, 4H), 4.08 (*t*, J = 6.0 Hz, 4H), 2.77 (*t*, J = 7.8 Hz, 2H), 1.50 (*t*, J = 7.8 Hz, 2H). ^{13}C NMR (125 MHz, DMSO-D_6, δ ppm): 178.63, 147.74, 142.63, 140.73, 127.63, 126.71, 125.78, 123.15, 123.06, 122.30, 120.63, 120.40, 118.15, 110.72, 110.42, 79.18, 39.19, 39.02, 38.61, 29.08, 19.08, 13.48. ^{11}B NMR (160 MHz, DMSO-D_6, δ ppm): −0.24, −0.35, −0.47, −0.58. ^{19}F NMR (470 MHz, DMSO-D_6, δ ppm) −137.91, −137.98, −139.41, −139.52 ESI–MS calcd. for $\mathbf{C_{43}H_{43}BF_2N_4O_4}^{2+}$ $[M + H]^+$ 729.33; found 729.34.

Synthesis of CPM–2

In a 50 mL round bottom flask, 0.65 mmol of **A2** and 0.29 mmol of **ALD–2** were dissolved in a minimum amount of DCM, and the flask was flushed with nitrogen. *n*-Butylamine (0.22 eq.) was then added dropwise to the reaction mixture *via* a syringe, and the reaction mixture was stirred overnight at room temperature. After completion of the reaction a solid separated out; this was filtered through a Buchner funnel and washed with cold ethyl acetate and diethyl ether and dried under vacuum ∼73%. ^{1}H NMR (500 MHz, DMSO-D_6, δ ppm): 8.78 (s, 2H), 8.46 (d, J = 15.3 Hz, 2H), 8.20 (d, J = 7.7 Hz, 4H), 8.10 (d, J = 9.0 Hz, 2H), 7.89 (d, J = 9.0 Hz, 2H), 7.81 (*t*, J = 7.4 Hz, 2H), 7.68 (*t*, J = 7.5 Hz, 4H), 7.41 (s, 2H), 7.31 (d, J = 15.9 Hz, 2H), 4.73 (s, 2H), 3.61 (s, 4H), 2.64 (s, 2H), 2.36 (s, 4H). ^{13}C NMR (125 MHz, DMSO-D_6, δ ppm): 178.63, 147.74, 142.63, 140.73, 127.63, 125.78, 123.15, 123.06, 122.30, 120.63, 120.40, 118.15, 110.72, 110.42, 79.18, 39.19, 39.02, 38.61, 29.08, 19.08, 13.48. ^{11}B NMR (160 MHz, DMSO-D_6, δ ppm): −2.26. ^{19}F NMR (470 MHz, DMSO-D_6, δ ppm): −137.32, −148.14 ESI–MS calcd. For $\mathbf{C_{40}H_{34}B_2F_4N_2O_5}^{2+}$ $[M + H]^+$ 721.32; found 721.31.

Results and discussion

BF_2bdk complexes **CPM–1** and **CPM–2** have been synthesized in good yields by condensation of the corresponding **ALD–1** and **ALD–2** with compounds **A1** and **A2**, following a very simple one step-reaction pathway (Scheme 1). These are air-stable, non-hygroscopic solids and possess good solubility in common organic solvents like I, DMF, and DMSO and moderate solubility in MeOH, EtOH, DCM, and EtOAc and are insoluble in water. The synthesized compounds have been well characterized by NMR (^{1}H, ^{13}C, ^{11}B and ^{19}F), ESI–MS, electronic absorption and emission spectroscopic studies and the spectral data have been given in the Experimental section and spectra shown in Fig. S1–S12 (ESI†) and Fig. 1 and 2.

Photophysical properties

The photophysical modulation by architectural alteration of the synthesized D–A molecules has been verified through UV–vis absorption and emission studies focusing on polarity sensitivity, viscochromism and TICT behavior. The absorption spectra of **CPM–1** and **CPM–2** have been recorded IACN (c = 30 μM), and display low energy absorption bands at 502 and 535 nm, respectively, attributed to π–π* transitions (Fig. 1). On the other hand, the characteristic high energy absorption bands corresponding to the acetylacetonate boron difluoride unit of **CPM–1**

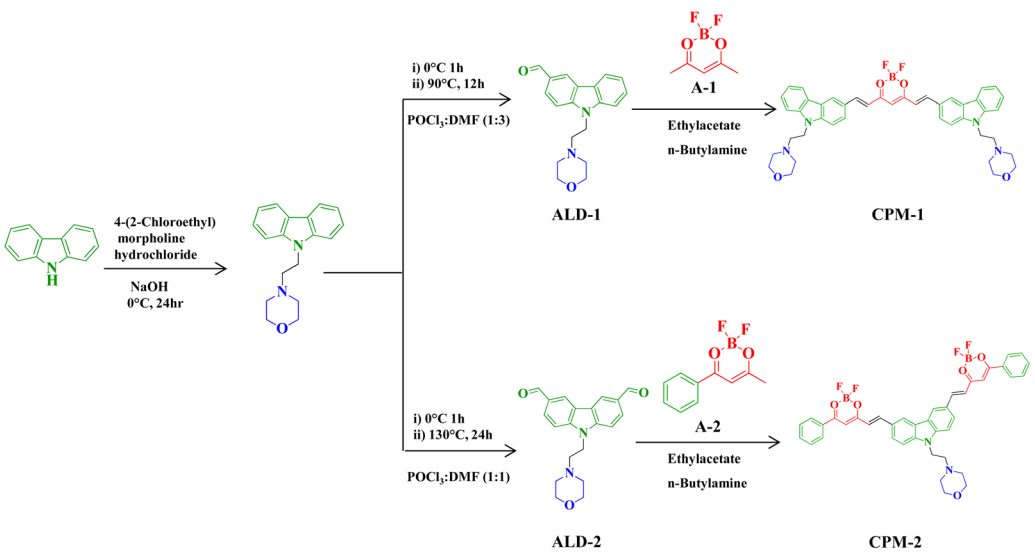

Scheme 1 Synthetic routes to **CPM–1** and **CPM–2**.

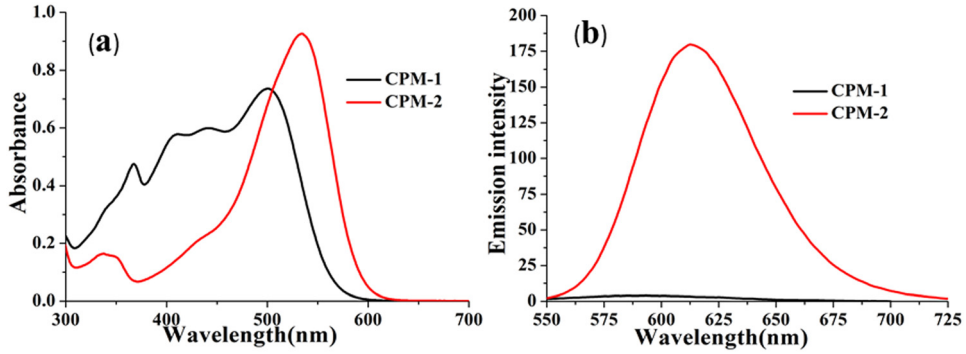

Fig. 1 UV–vis absorption (a) and emission (b) spectra of **CPM–1** and **CPM–2** in ACN (c = 30 μM).

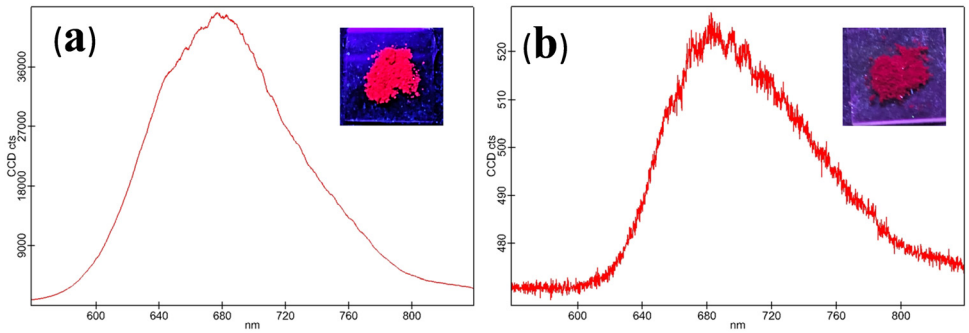

Fig. 2 Solid state emission spectrum of **CPM–1** (a) and **CPM–2** (b) (λ_{ex} = 502 and 535 nm, respectively). [Insets: solid state emission of **CPM–1** and **CPM–2** under UV light (λ_{ex} = 365 nm)].

and **CPM–2** were observable at 367 and 348 nm, respectively. A broad absorption band related to the morpholine-substituted carbazole units of **CPM–1** and **CPM–2** has been visualized at ∼ 438 nm. On the other hand in their emission profiles, **CPM–1** and **CPM–2** exhibited emission peaks at 594 and 613 nm upon excitation at 502 and 535 nm, respectively (Fig. 1). The Stokes' shifts for **CPM–1** and **CPM–2** were measured at 3085 cm^{-1} and 2378 cm^{-1}, respectively. Furthermore, the fluorescence quantum yield (Φ_f) of **CPM–1** was found to be considerably lower (Φ_f = 0.3%) as compared to **CPM–2** (Φ_f = 10%).

Furthermore, solid state photoluminescence spectra of **CPM–1** and **CPM–2** have also been recorded (Fig. 2). **CPM–1** showed a broad band (600–800 nm) with a maximum centered at ∼680 nm; on the other hand, **CPM–2** displayed a similar type of band (630–800 nm) with a maximum centered at ∼685 nm. Interestingly the solid state emission intensity of **CPM–1** was found to be much higher relative to **CPM–2,** which can further be visualized under a UV lamp (Fig. 2: inset, λ_{ex} = 365 nm).

The initial indication for the effect of the altered D–A architecture can be realized by more red shifted absorption and emission of **CPM–2** as well as lower Φ_f (solution) of **CPM–1**. However, a more systematic study of ICT behavior needs to be monitored to establish a comparative account in terms of photophysical attributes for A–D–A and D–A–D constructs.

In this context, the comparative ICT behavior of **CPM–1** and **CPM–2** has further been monitored through study of their solvatochromic behavior. In light of this, we investigated these D–A systems across a range of organic solvents with varying polarities, including benzene, toluene, 1,4-dioxane, $CHCl_3$, THF, CH_2Cl_2 and CH_3CN. The absorption spectra of the compounds displayed insignificant changes with different solvent polarities (Fig. S14–S15, ESI†), indicating that the ground state of the luminophores is eventually unaffected by solvent polarity. However, the emission spectra exhibited considerable changes in response to the solvent polarity, ranging from benzene to CH_3CN. Specifically, for **CPM–1** and **CPM–2**, a positive solvatochromism with bathochromic shifts of 33 nm and 47 nm, respectively, was observed, upon going from extreme non-polar to extreme polar solvents. The shift was accompanied by considerable emission quenching as well as broadening and loss of the vibronic structure of the emission spectra (Fig. 3) indicating strong ICT behavior. Furthermore, the Lippert–Mataga plots between Stokes' shifts and orientolarizabilitybility (Δf) for **CPM–1** and **CPM–2** displayed linear dependency of the positive slope on Stokes' shift, which further denotes positive solvatochromism (Fig. S13, ESI†).

Additionally, Φ_f has also been calculated in solvents of different polarity and the data have been summarized in Table S1 (ESI†). The Φ_f values for **CPM–1** and **CPM–1** were found to be the maximum in non-polar solvents, while Φ_f decreases rapidly with increasing solvent polarity owing to the stabilization of the transferred charge within the molecules. The solvent effect was further assessed through evaluation of excited state dynamics under the effect of differential polarity

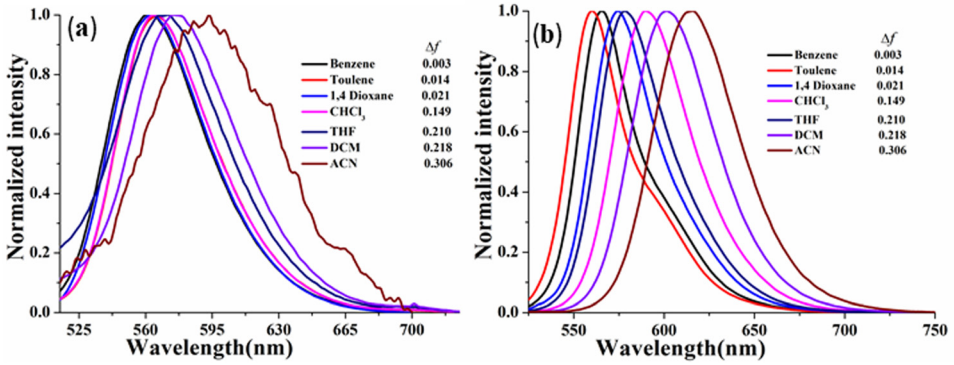

Fig. 3 Normalized emission spectra of **CPM–1** (a) and **CPM–2** (b) (c = 30 μM) in solvents of varying polarity.

(Fig. S16, ESI†). The radiative (k_r) and nonradiative (k_{nr}) decay rate constants from the excited singlet state (S_1) have been calculated and the data have been compared (Table S1, ESI†). In general, the k_r values decrease with increasing solvent polarity; however the comparative k_r and k_{nr} values of **CPM–1** and **CPM–2** in $CHCl_3$ were found to be responsible for their significant Φ_f in $CHCl_3$. On the other hand the high k_{nr} and low k_r can be responsible for very low quantum yields of **CPM–1** and **CPM–2** in CH_3CN. Interestingly the effect of solvent on the k_r and k_{nr} values was more pronounced in **CPM–2** relative to **CPM–1**.

Thus, the solvatochromic study professes the superior ICT behvaiour of **CPM–2** (A–D–A) relative to **CPM–1** (D–A–D) and strengthens our assumption of tuning of photophysical behavior through structural modulations.

The effectiveness of the above-mentioned approach has been revealed by manifestation of the TICT state as reflected through emission spectra of **CPM–1** and **CPM–2** in a mixture of tetrahydrofuran (THF) and *n*-hexane (Fig. 4 and Fig. S17, ESI†), with increasing *n*-hexane fractions (f_H). As expected, in accordance with the characteristics of conventional D–A molecules, both the fluorphores exhibited blue-shifted emission with gradual addition of *n*-hexane. However, **CPM–1** displayed a hypsochromic shift of only 7 nm; however a more significant blue shift of 41 nm was observable for **CPM–2** at f_H = 90%. These compelling observations firmly indicated the stronger dipolar ICT character of A–D–A (**CPM–2**) relative to D–A–D (**CPM–1**).

Viscochromism and restricted intramolecular rotation

The viscosity sensitivity of the designed probes has been verified through recording the emission spectra in glycerol–methanol mixtures by varying the percentage of glycerol (Fig. 5). **CPM–1** exhibited significant emission enhancement (~2.5 fold) upon increasing the f_g from 0 to 99% for the emission maxima at 586 nm in methanol. The emission enhancement can be attributed to restriction of intramolecular rotation followed by deactivation of non-radiative channels. On the other hand, no such emission enhancement was observable for **CPM–2** (Fig. S18, ESI†). In addition, the viscochromism has further been authenticated through fluorescence lifetime measurements. It was observed that the fluorescence life time increased from 0.11 ns (f_g = 0%) to 0.31 ns (f_g = 90%) supporting the emission enhancement. These observations cumulatively established **CPM–1** as an effective molecular rotor, which can be explored for lysosomal targeting.

As is well known, TICT is achieved through intramolecular rotation or twisting and leads to red-shifted and quenched

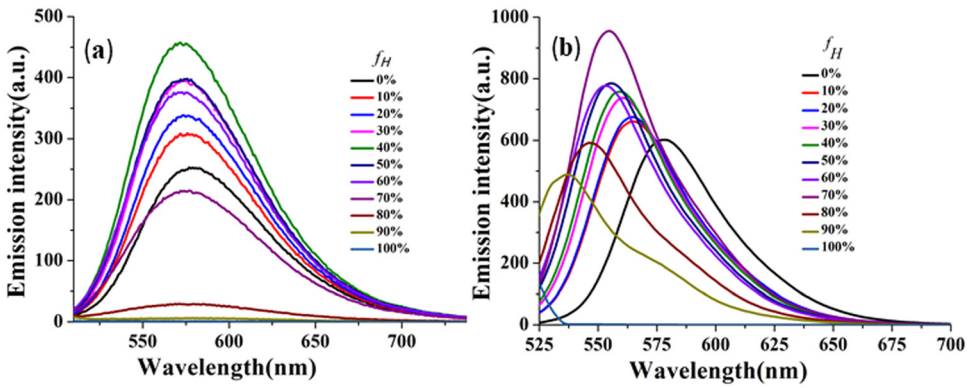

Fig. 4 Emission spectra of **CPM–1** (a) and **CPM–2** (b) in THF and THF/*n*-hexane mixtures (c = 30 μM) with increasing fractions of *n*-hexane and formation of the TICT state.

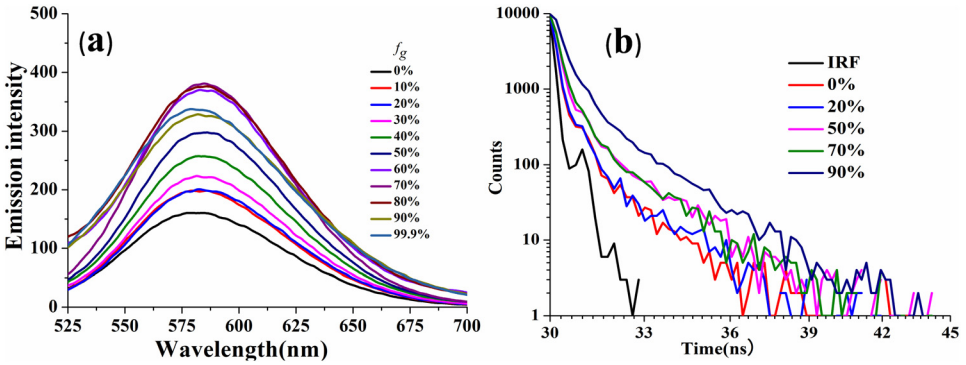

Fig. 5 Emission spectra of **CPM–1** (a) and time-resolved fluorescence decay of **CPM–1** (b) in MeOH and MeOH/glycerol mixtures (c = 30 μM) with increasing fractions of glycerol.

emission. On the other hand, blocking of intramolecular rotations in the aggregated state leads to fixed molecular conformations, which might further lead to emission enhancement. Both processes are competitive and define the emission in D–A construct-based AIEgens.[64–66]

One of the most compelling outcomes of the detailed photophysical study of **CPM–1** and **CPM–2** lies in epistemic interdependence of restriction of intramolecular rotations (RIRs) and TICT. The pragmatic aspects of evidence are demonstrated by an effective RIR but weak TICT in **CPM–1,** while contrasting properties are found in **CPM–2,** which displays a non-existent RIR and very effective TICT. These explicit evidences establish a design rationale for photophysical modulation *via* structural modifications.

Density functional theory calculations

The present study focuses on the theoretical investigation of geometrical optimization for (D–A–D) and (A–D–A) systems using the B3LYP method with the 6–31G** basis set. Fig. 6 illustrates the distribution of the highest occupied molecular orbitals (HOMOs) and the lowest unoccupied molecular orbitals (LUMOs) for **CPM–1** and **CPM–2**. It can be observed that the HOMOs are predominantly located on the respective carbazole and morpholine units, which act as the donor moieties. Conversely, the LUMOs are primarily concentrated over the BF_2 core, serving as the acceptor moieties. The energy difference values between the HOMO−2, HOMO−1 and LUMO, known as the band gap, are found to be 3.44 eV for **CPM–1** and 3.25 eV for **CPM–2,** respectively. The HOMO−2 and HOMO−1 energy levels are −5.85 eV for **CPM–1** and 6.09 eV for **CPM–2,** respectively, while the LUMO energy levels are −2.41 eV for **CPM–1** and −2.84 eV for **CPM–2**. The substantial spatial separation between the HOMO−2, HOMO−1 and LUMO suggests the possibility of an ICT phenomenon between the donor and acceptor moieties, corroborating the experimental observations (*vide infra*). Furthermore, the UV–vis spectra of **CPM–1** and **CPM–2** were obtained from TD–DFT calculations (Fig. S20 and

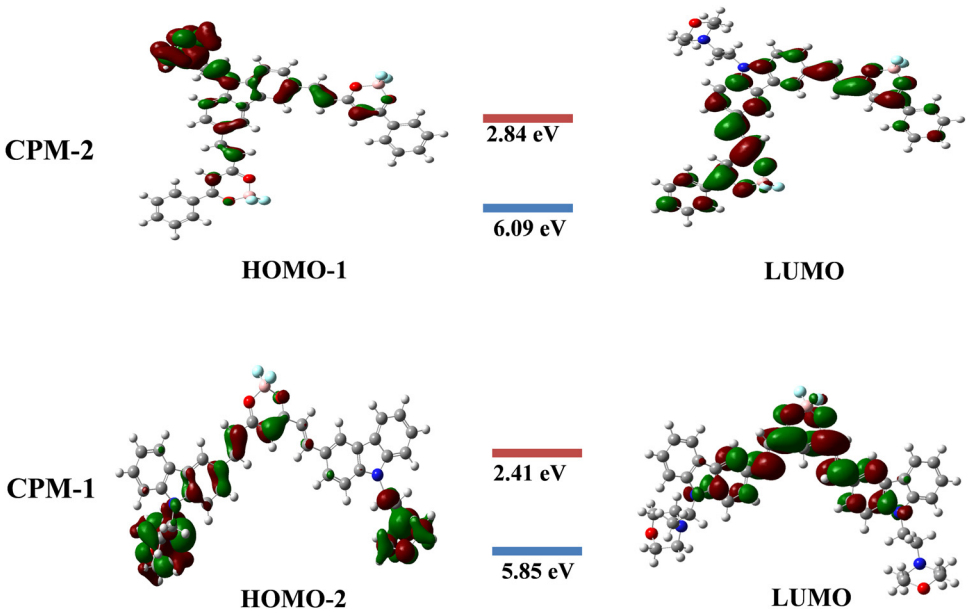

Fig. 6 The HOMO–LUMO frontier molecular orbital (FMO) diagrams of **CPM–1** and **CPM–2**.

Table S3, ESI†). Table S3 (ESI†) summarizes the details of the absorption wavelength, energy, oscillation strength (f), assignment, and transitions.

The TD–DFT calculations reveal that, for both **CPM–1** and **CPM–2**, the HOMO−2 → LUMO and HOMO−1 → LUMO transitions, respectively, contribute significantly to the ICT process, accounting for 95% in **CPM–1** and 97% in **CPM–2**. The dipole moments of **CPM–1** and **CPM–2** in the ground state were found to be 13.08 and 12.37 Debye, respectively, which increased to 19.05 and 18.48 in the excited state. An increase in the dipole moment was noted in the excited state, which was in good agreement with the observed solvatochromism and the anticipated charge separation. These theoretical findings provide valuable insights into the electronic structure and optical properties of the investigated D–A–D and A–D–A systems. The results not only support the experimental observations but also shed light on the potential for intramolecular charge transfer in these systems, which can have implications for various applications in optoelectronic devices.

Application to lysosome tracking *in vivo*

The applicability of the developed fluorophores in biological systems has been realized through lysosome tracking experiments. In order to assess the toxic effects of **CPM–1** on *Drosophila*, flies were administered with concentrations of 5 μM, 50 μM, and 100 μM.

The results revealed that **CPM–1** at concentrations of 5 μM and 50 μM exhibited lower toxicity, which is non-significant, as evidenced by the successful eclosion of 92% and 87% of the adult flies compared to the control group (Fig. 7A). However, at a concentration of 100 μM, **CPM–1** was found to be toxic to fly development, with a reduced eclosion rate; hence, the 50 μM concentration is the safe dose for oral administration. The cell viability of larval gut tissue treated with the **CPM–1** formulation was assessed using the MTT (3-[4,5-dimethylthiazol-2-yl]-2,5 diphenyl tetrazolium bromide) assay. The results demonstrated that larvae treated with **CPM–1**of 5 μM and 25 μM concentrations presented 95.5% and 73.7% viability, respectively. However, at a concentration of 50 μM, the viability decreased to only 65% (Fig. 7B). These findings indicate that the viability of the larval gut tissue is dose-dependent, with higher concentrations of **CPM–1** leading to reduced cell viability.

CPM–1 colocalization with Lyso-Tracker Green

The colocalization experiment performed in the gut tissu[e] of 3rd instar *Drosophila* larvae involved comparing the fluorescence patterns of **CPM–1** and LumiTracker Lyso Green to assess the specificity of **CPM–1** for tracking the lysosomes. The results showed that the red fluorescence emitted by **CPM–1** (Fig. 8a and d) colocalized with the green fluorescence emitted by LumiTracker Lyso Green (Fig. 8b and e) and the merged images (Fig. 8c and f) showed absolute colocalization in the corresponding lysosomal regions. The colocalization of **CPM–1** (red fluorescence) and LumiTracker Lyso Green (green fluorescence) indicated that **CPM–1** specifically targets and localizes to lysosomes in the gut tissue of *Drosophila* larvae. The magnitude of the Pearson coefficient is 0.741, indicating a high correlation between the variables (Fig. 8g, h and i). The coincidence of the fluorescence signal suggests that **CPM–1** is a reliable marker for visualizing and studying lysosomes in this experimental *in vivo* model.

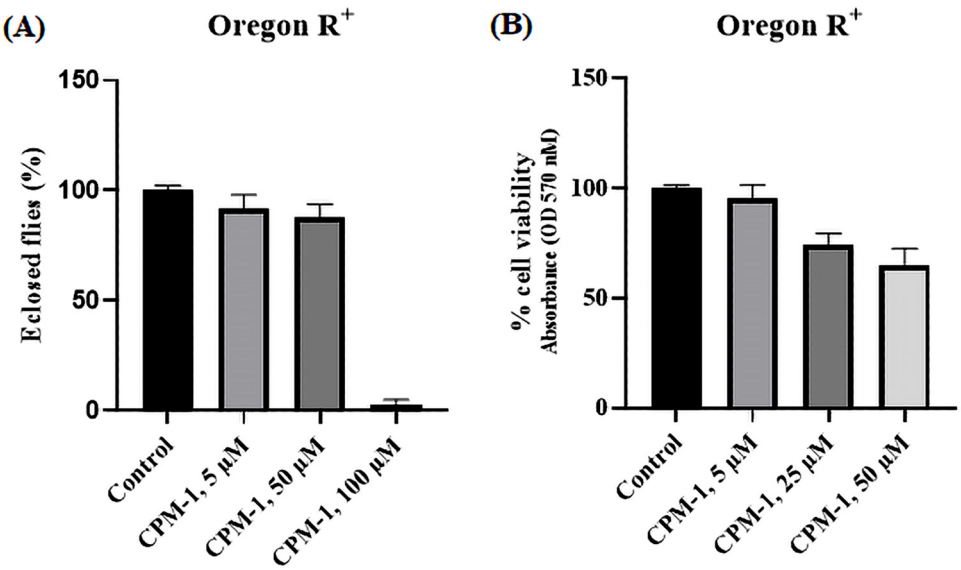

Fig. 7 In histogram (A), the percentage of flies that eclosed during the toxicity assay after **CPM–1** treatment is presented. Histogram (B) illustrates the percentage of cell viability following the MTT assay of **CPM–1**-treated larval gut tissue.

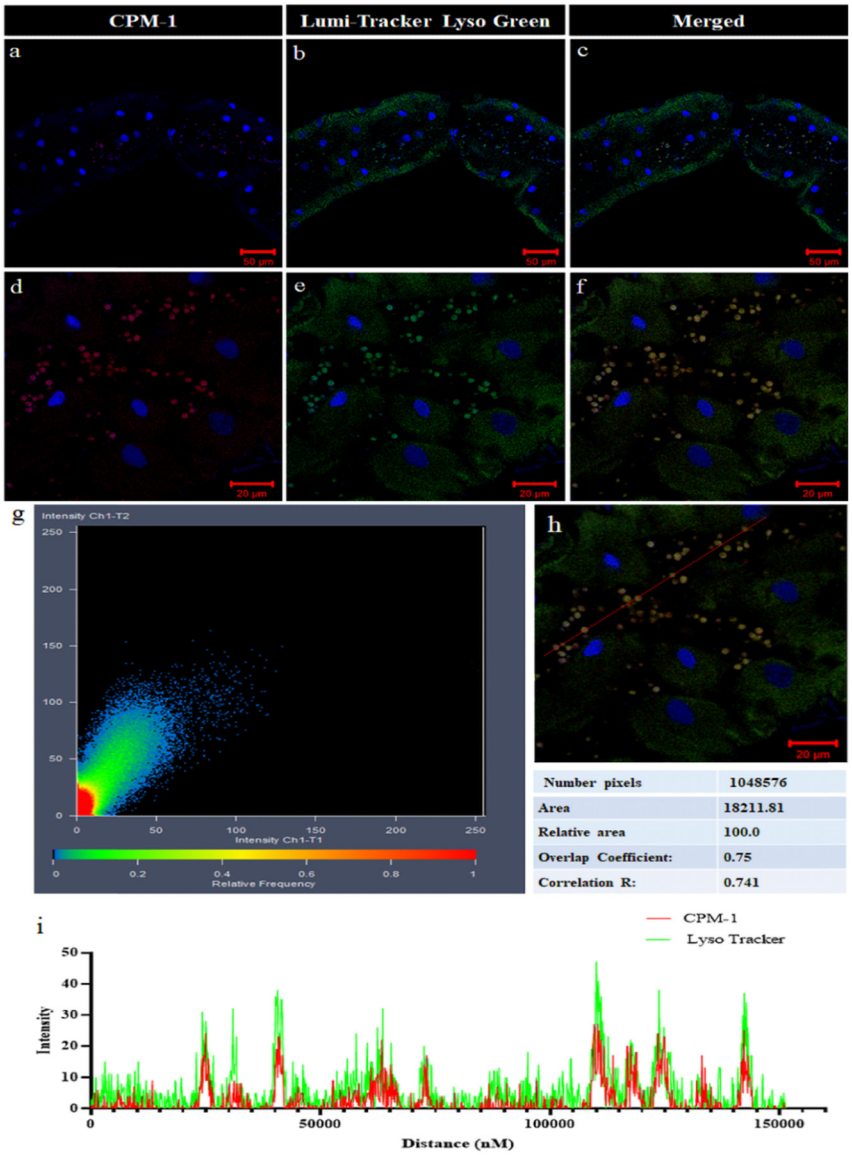

Fig. 8 Confocal micrographs of 1 μM **CPM–1** (panels a and d) and LumiTracker Lyso Green at 1 μM (panels b and e). (Panels c and f) represent the merged images, showing the co-localization of **CPM–1** and LumiTracker Lyso Green. Panel (g) shows the correlation scatter plot of panel (f) and graph (i) the relative intensity correlation of panel (h).

Conclusions

In summary, we present an empirical strategy that prioritizes the architectural alterations to achieve desired photophysical properties through the development of unconventional D–A molecules **CPM–1** and **CPM–2**. The meticulously designed D–A molecules bearing D–A–D and A–D–A constructs displayed distinct photophysical properties. The study of the competitive RIR and TICT behavior reflects a weaker ICT with a more effective RIR in **CPM–1,** while a stronger TICT and non-existent RIR in **CPM–2**. These contrasting properties have been accompanied by strong NIR emission in the solid state by both the molecules, which is reminiscent of their inherent D–A constructs. Owing to its intricate structural attributes and excellent viscosity sensitivity, **CPM–1** has been explored for its lysosome tracking ability wherein it displayed selective lysosomal localization in larval gut tissue of wild-type *Drosophila* flies. The proposed hypothesis of architectural control can be used to provide more in-depth understanding of competitive photophysical properties of D–A molecules and get the desired applications.

Conflicts of interest

The authors declare no competing financial interests.

Acknowledgements

The authors gratefully acknowledge the Science and Engineering Research Board (SERB), New Delhi, India (Scheme

ECR/2018/001810) and BHU IOE cell (Seed/Incentive Grant) for providing financial assistance.

References

1 Z. Guo, Z. Jin, J. Wang and J. Pei, *Chem. Commun.*, 2014, **50**, 6088–6090.
2 Q. Zhao, H. Xiao, F. Yang, Y. Wang, P. Li and Z. Zheng, *Pharmacol. Res. Commun.*, 2023, **188**, 106627.
3 J. Cheng, *Biomolecules*, 2015, **5**, 1099–1121.
4 Z. Zhang, P. Yue, T. Lu, Y. Wang, Y. Wei and X. Wei, *J. Hematol. Oncol.*, 2021, 79.
5 K. K. Mahapatra, S. R. Mishra, B. P. Behera, S. Patil, D. A. Gewirtz and S. K. Bhutia, *CMLS*, 2021, **78**, 7435–7449.
6 S. R. Bonam, F. Wang and S. Muller, *Nat. Rev. Drug Discovery*, 2019, **18**, 923–948.
7 K. Pal, P. Kumar and A. P. Koner, *J. Photochem. Photobiol., B*, 2019, **206**, 111848.
8 B. Jana, S. Jin, E. M. Go, Y. Cho, D. Kim, S. Kim, S. K. Kwak and J. Ryu, *J. Am. Chem. Soc.*, 2023, **145**, 18414–18431.
9 S. Rafiq, S. L. McKenna, S. Muller, M. P. Tschan and M. Humbert, *Leukemia*, 2021, **35**, 2759–2770.
10 C. Kong, Y. Li, Z. Liu, J. Ye, Z. Wang, L. Zhang, W. Kong, H. Liu, H. Pang, Z. Hu, J. Gao and F. Qian, *ACS Nano*, 2019, **13**, 4049–4063.
11 Y. Song, H. Zhang, X. Wang, X. Geng, Y. Sun, J. Liu and Z. Li, *Anal. Chem.*, 2021, **93**, 1786–1791.
12 Y. Wei, X. Weng, X. Sha, R. Sun, Y. Xu and J. Ge, *Sens. Actuators, B*, 2021, **326**, 128954.
13 L. Wang, Y. Xiao, W. Tian and L. Deng, *J. Am. Chem. Soc.*, 2013, **135**, 2903–2906.
14 A. Tantipanjaporn, K. K. Y. Kung, W. C. Chan, J. R. Deng, B. C. B. Ko and M. K. Wong, *Sens. Actuators, B*, 2022, **367**, 132003.
15 Y. H. Zhan, X. J. Li, R. Sun, Y. Xu and J. Ge, *Anal. Chim. Acta*, 2016, **933**, 175–181.
16 J. Zhang, Q. Chen, Y. Fan, H. Qiu, Z. Ni, Y. Li and S. Yin, *Dyes Pigm.*, 2021, **193**, 109500.
17 B. Feng, Y. Ma, F. Zheng, Y. Huang, X. Feng, K. Zhang, L. Liu and W. Zeng, *J. Chem. Eng.*, 2023, **464**, 142554.
18 N. Choi, J. Lee, E. Park, J. Lee and J. Lee, *Molecules*, 2021, **26**, 217.
19 J. Hong, Q. Li, Q. Xia and G. Feng, *Anal. Chem.*, 2021, **93**, 16956–16964.
20 Y. Song, H. Zhang, X. Wang, X. Geng, Y. Sun, J. Liu and L. Zhaohui, *Anal. Chem.*, 2021, **93**, 1786–1791.
21 Q. Liu, C. Liu, X. Jiao, S. Cai, S. He, L. Zhao, X. Zeng and T. Wang, *Dyes Pigm.*, 2012, **190**, 109293.
22 J. Li, X. Li, J. Jia, X. Chen, Y. Lv, Y. Gua and J. Li, *Dyes Pigm.*, 2019, **166**, 433–442.
23 M. Grossi, M. Morgunova, S. Cheung, D. Scholz, E. Conroy, M. Terrile, A. Panarella, J. C. Simpson, W. M. Gallagher and D. F. O. Shea, *Nat. Commun.*, 2016, **7**, 10855.
24 J. M. Li, F. F. Xiang, D. H. Zhou, J. X. Xu, H. Zhang, Y. Z. Liu, Q. Q. Kong, X. Q. Yu and K. Li, *Chem. Biomed. Imaging*, 2023, **2**, 126–134.
25 Z. Li, Y. Pei, Y. Wang, Z. Lu, Y. Dai, Y. Duan, Y. Ma and H. Guo, *J. Org. Chem.*, 2019, **84**, 13364–13373.
26 R. Mengji, C. Acharya, V. Vangala and A. Jana, *Chem. Commun.*, 2019, **55**, 14182.
27 Q. Liu, C. Lib, X. Jiao, S. Cai, S. Hb, L. Zhao, X. Zeng and T. Wang, *Dyes Pigm.*, 2021, **190**, 109293.
28 P. Cheng, X. Du, S. Chen, K. Chen, Y. Yuan, J. Shao, Q. Shen, P. Sun and Q. Fan, *ACS Appl. Nano Mater.*, 2023, **6**, 10736–10745.
29 J. Li, A. Ji, M. Lei, L. Xuan, R. Song, X. Feng, H. Lin and H. Chen, *J. Med. Chem.*, 2023, **66**, 7880–7893.
30 T. Han, Y. Wang, J. Xu, N. Zhu, L. Bai, X. Liu, B. Sun, C. Yu, Q. Meng, J. Wang, Q. Su, Q. Cai, K. S. Hettie, Y. Zhang, S. Zhu and B. Yang, *Chem. Sci.*, 2022, **13**, 13201–13211.
31 X. Yang, C. Li, L. Liu, H. Zhang, H. T. Feng, Y. Li, G. Jiang and J. Wang, *New J. Chem.*, 2022, **46**, 9819–9824.
32 Y. Sugihara, N. Inai, M. Taki, T. Baumgartner, R. Kawakami, T. Saitou, T. Imamura, T. Yanai and S. Yamaguchi, *Chem. Sci.*, 2021, **12**, 6333–6341.
33 T. Kim, W. Kim, H. Mori, A. Osuka and D. Kim, *J. Phys. Chem. C*, 2018, **122**, 19409–19415.
34 A. K. Gupta, A. Kumar, R. Singh, M. Devi, A. Dhir and C. P. Pradeep, *ACS Omega*, 2018, **3**, 14341–14348.
35 J. Shaya, P. R. Corridon, B. Al-Omari, A. Aoudi, A. Shunnar, M. I. H. Mohindeen, A. Qurashi, B. Y. Michel and A. Burger, *J. Photochem. Photobiol., C*, 2022, **52**, 100529.
36 Z. Xiang, Z. Y. Wang, T. B. Ren, W. Xu, Y. Liu, X. Zhang, P. Wu, L. Yuan and X. Zhang, *Chem. Commun.*, 2019, **55**, 11462–11465.
37 D. B. Biernacka, S. G. Mucha, L. Firlej, F. Formalik, J. L. Bantignies, E. Anglaret, M. Samoc and K. Matczyszyn, *ACS Appl. Mater. Interfaces.*, 2023, **15**, 32717–32731.
38 E. Horak, M. Robic, A. Simanovic, V. Mandic, R. Vianello, M. Hranjec and I. M. Steinberg, *Dyes Pigm.*, 2019, **162**, 688–696.
39 R. Singh, A. K. Gupta and C. P. Pradeep, *Cryst. Growth Des.*, 2021, **21**, 1062–1076.
40 Z. Lia, Y. Hub, K. Zhang, Y. Zhang, Q. Q. Hu, X. J. Zhang, X. K. Zhang and Y. P. Zhu, *Dyes Pigm.*, 2020, **182**, 108686.
41 Z. Li, Y. Pei, Y. Wang, Z. Lu, Y. Dai, Y. Duan, Y. Ma and H. Guo, *J. Org. Chem.*, 2019, **84**, 13364–13373.
42 A. D'Aléo, A. Felouat, V. Heresanu, A. Ranguis, D. Chaudanson, A. Karapetyan, M. Giorgic and F. Fages, *J. Mater. Chem. C*, 2014, **2**, 5208–5215.
43 C. A. DeRosa, S. Hiroto and C. L. Fraser, *J. Phys. Chem. C*, 2019, **123**, 20488–20496.
44 T. Butler, M. Zhuang and C. L. Fraser, *J. Phys. Chem. C*, 2018, **122**, 19090–19099.
45 T. Butler, W. A. Morris, J. S. Kosicka and C. L. Fraser, *ACS Appl. Mater. Interfaces*, 2016, **8**, 1242–1251.
46 X. Zhang, Y. Tian, H. Zhang, A. Kavishwar, M. Lynes, A. L. Brownell, H. Sun, Y. H. Tseng, A. Moore and C. Ran, *Sci. Rep.*, 2015, **5**, 13116.
47 X. Zhang, Y. Tian, Z. Li, X. Tian, H. Sun, H. Liu, A. Moore and C. Ran, *J. Am. Chem. Soc.*, 2013, **135**, 16397–16409.
48 A. Chaicham, S. Kulchat, G. Tumcharern, T. Tuntulani and B. Tomapatanaget, *Tetrahedron*, 2010, **66**, 6217–6223.

49 G. Zhang, S. H. Kim, R. E. Evans, B. H. Kim, J. N. Demas and C. L. Fraser, *J. Fluoresc.*, 2009, **19**, 881–889.
50 S. B. Ebrahimi, D. Samanta and C. A. Mirkin, *J. Am. Chem. Soc.*, 2020, **142**, 11343–11356.
51 H. Cheng, X. Cao, S. Zhang, K. Zhang, Y. Cheng, J. Zhao, L. Zhou, X. Liang and J. Yoon, *Adv. Mater.*, 2022, **35**, 2207546.
52 M. Grossi, M. Morgunova, S. Cheung, D. Scholz, E. Conroy, M. Terrile, A. Panarella, J. C. Simpson, W. M. Gallagher and D. F. Shea, *Nat. Commun.*, 2016, **7**, 1–13.
53 P. C. Saha, T. Chatterjee, R. Pattanayak, R. S. Das, A. Mukherjee, M. Bhattacharyya and S. Guha, *ACS Omega*, 2019, **4**, 14579–14588.
54 V. N. Nguyen and H. Li, Recent Development of Lysosome-Targeted Organic Fluorescent Probes for Reactive Oxygen Species, *Molecules*, 2023, **28**, 6650.
55 P. Z. Chen, L. Niu, Y. Chen and Q. Yang, *Coord. Chem. Rev.*, 2017, **350**, 196–216.
56 W. Liu, Y. Wang, G. Ge, L. Ma, L. Ren and Y. Zhang, *Dyes Pigm.*, 2019, **171**, 107704.
57 N. Liu, P. Z. Chen, J. Wang, L. Niu and Q. Yang, *Chin. Chem. Lett.*, 2019, **30**, 1939–1941.
58 H. Rai, S. Gupta, S. Kumar, J. Yang, S. K. Singh, C. Ran and G. Modi, *J. Med. Chem.*, 2022, **65**, 8550–8595.
59 K. K. Laali, A. T. Zwarycz, S. D. Bunge, G. L. Borosky, M. Nukaya and G. D. Kennedy, *ChemMedChem*, 2019, **14**, 1173–1184.
60 D. D. Perrin, W. L. F. Armango and D. R. Perrin, *Purification of laboratory Chemicals*, Pergamon, Oxford, UK, 1986.
61 A. D'Aleó, M. H. Sazzad, D. H. Kim, E. Y. Choi, J. W. Wu, G. Canard, F. Fages, J. C. Ribierre and C. Adachi, *Chem. Commun.*, 2017, **53**, 7003–7006.
62 T. Kim, W. Kim, H. Mori, A. Osuka and D. Kim, *J. Phys. Chem. C*, 2018, **122**, 19409–19415.
63 Z. F. Fang, F. W. Pei, Z. J. Chao, L. S. Hui, Q. X. Ying and W. S. Xiang, *Indian J. Chem.*, 2016, **55**, 713–717.
64 R. S. Singh, S. Mukhopadhyay, A. Biswas and D. S. Pandey, *Chem. – Eur. J.*, 2016, **22**, 753–763.
65 H. Li, Y. Guo, G. Li, H. Xiao, Y. Lei, X. Huang, J. Chen, H. Wu, J. Ding and Y. Cheng, *J. Phys. Chem. C*, 2015, **119**, 6737–6748.
66 N. Zhao, Z. Yang, J. W. Y. Lam, H. H. Y. Sung, N. Xie, S. Chen, H. Su, M. Gao, I. D. Williams, K. S. Wong and B. Z. Tang, *Chem. Commun.*, 2012, **48**, 8637–8639.

